University of Bath

Alternative formats

If you require this document in an alternative format, please contact:
openaccess@bath.ac.uk

A coupled Particle-In-Cell (PIC)-Discrete Element Method (DEM) solver for fluid-solid mixture flow simulations

Qiang Chen[a,b], Chongwei Zhang[b], Jun Zang[a,b,*], Dezhi Ning[b]

[a]*Research Unit for Water, Environment and Infrastructure Resilience (WEIR), Department of Architecture and Civil Engineering, University of Bath, BA2 7AY, U.K.*
[b]*State Key Laboratory of Coastal and Offshore Engineering, Dalian University of Technology, Dalian, 116024, China*

Abstract

In this paper, a coupled Particle-In-Cell (PIC)-Discrete Element Method (DEM) model is developed for numerical simulations of complex fluid-solid mixture flows. The fluid-solid interaction part is solved using the hybrid Eulerian-Lagrangian PIC model, and the solid-solid interaction part is simulated using the Lagrangian DEM model. The PIC model gives the coupled PIC-DEM model both Eulerian efficiency and Lagrangian flexibility, compared to purely Lagrangian methods such as Smoothed Particle Hydrodynamics (SPH). The time step difference between the PIC model and the DEM model is handled using the idea of subcycles. In addition, a straightforward method is proposed for mitigating the issue of unphysical gaps between solids during collision due to the use of the Cartesian cut cell method for fluid-solid interaction. The PIC-DEM model is validated by physical experiments of the collapse of solid cylinder layers with and without water. Following that, the capability of the numerical model is further demonstrated through a more complex problem of solid dumping through fall pipes. The results show great potential of the PIC-DEM model being a useful tool for simulating complex fluid-solid mixture flows.

Keywords: Particle-In-Cell (PIC) method, Discrete element method (DEM), fluid-solid mixture flows, fall-pipe solid dumping

1. Introduction

Numerical simulation of fluid-solid mixture flows, typically involving large number of solids, remains an important challenge in a number of engineering disciplines such as coastal

---

*Corresponding author.

   Email addresses: `chenqiang913@hotmail.com` (Qiang Chen), `j.zang@bath.ac.uk` (Jun Zang)

and offshore engineering. For example, floating foams are being investigated as an anti-sloshing technique for oil and liquefied natural gas (LNG) transport (Zhang et al., 2019). Numerical modelling in such area involves complex coupling amongst fluid-fluid, fluid-solid and solid-solid interactions. The numerical time steps required for modelling each phase vary significantly due to different interaction mechanisms. In addition, difficulties arise in dealing with numerical schemes such as free-surface tracking/capturing, solution of the advection term, fluid-solid interface tracking/capturing and solid-solid collisions. Traditional methods for such simulations are usually purely Lagrangian; for example, meshless fluid models, such as Smoothed Particle Hydrodynamics (SPH) (Violeau and Rogers, 2016), are typically coupled with the Lagrangian Discrete Element Method (DEM) model for solids (Cundall and Strack, 1979). However, the Lagrangian nature has made these methods computationally very expensive. It is therefore desired that Eulerian methods are to be incorporated into such coupling methods for numerical efficiency, which is the aim of this paper.

Despite being traditionally very expensive, meshless methods such as SPH (Violeau and Rogers, 2016) and moving particle semi-implicit (MPS) method (Koshizuka and Oka, 1996) are more suitable for simulating complex fluid flows, compared to conventional grid-based Eulerian methods. This is because meshless methods are natural in tracking free surfaces (particularly with large deformations) and solving any transport terms (He et al., 2018). Moreover, the fluid-solid interface is always clearly represented in the calculations of these meshless models (Zhang et al., 2009). Since the DEM is also fully Lagrangian, many researchers focusing on meshless method, particularly the SPH method, have made efforts to couple such fluid models with DEM for simulating complex fluid-solid mixture flows (see e.g. Zhang et al. (2009); Canelas et al. (2016); He et al. (2018)). The fully Lagrangian DEM (Cundall and Strack, 1979) has become very popular for solid-solid interaction in many engineering fields since its invention. The use of the overlap between solids for calculating contact forces has made this method efficient in both CPU time and memory storage requirement. A comprehensive review of the DEM for simulations of complex granular flows can be found in Guo and Curtis (2015).

Earlier attempts to involve Eulerian methods for fluid-solid mixture flow simulations can be found in the works of Glowinski et al. (1999) and Patankar et al. (2000), where the Distributed Lagrangian multiplier (DLM) method has been developed for fluid-solid interactions. However, no free surface was considered in these simulations. Recently, Chen et al. (2016) developed a Particle-In-Cell (PIC) method based solver for simulating wave interaction with floating bodies in the maritime engineering field. The PIC method was ini-

2

tially developed in an attempt to combine the advantages of both Eulerian and Lagrangian methods for fluid flows (Harlow, 1964). It features from a combined use of Lagrangian particles and Eulerian grid. In particular, the particles are used to solve the transport terms and track the free-surface position for Lagrangian flexibility, while the gird is employed for solving the non-advection terms for computational efficiency. One of the primary benefits arising from the particle nature of the PIC method is that this method incorporates the flexibility and accuracy of meshless methods in terms of handling large free-surface deformations and solving the transport terms. Another benefit due to the grid nature is that it is very convenient to incorporate any grid-based optimised numerical schemes in PIC. This is because the main calculations, such as the enforcement of incompressibility and boundary conditions, are on the background grid. For more details and recent developments on the PIC method, the reader is referred to the works of Edwards and Bridson (2012), Maljaars et al. (2018) and Chen et al. (2019). In this paper, we further extend the PIC model of Chen et al. (2016) to simulate complex fluid-solid mixture flows (with free surface) through coupling with a DEM model. The coupled model is referred to as PIC-DEM hereafter. The aim, as mentioned above, is to take advantage of the hybrid Eulerian-Lagrangian nature of the PIC method to improve numerical efficiency. Note that despite being hybrid, the main computations of the PIC part are on an Eulerian grid. Hence, numerical efficiency can be expected; in fact, with new innovations, the PIC method could be several orders faster than SPH (Violeau and Rogers, 2016; Chen, 2017).

The paper is organised as follows: Section 2 gives an overview of the PIC-DEM model. Next, in Section 3 the numerical model is first validated against an existing experiment of the collapse of multiple solid cylinder layers with and without water. Then, an extension numerical study on fall-pipe solid dumping is conducted. Finally, in Section 4 conclusions are drawn.

2. Numerical Model

In the PIC-DEM model developed for fluid-solid mixture flows, the fluid-solid interaction part is resolved using the PIC model and the solid-solid interaction part is computed by the DEM model. In the following subsections, the PIC model, the DEM model and the coupling algorithm for the PIC-DEM model are introduced. In this paper, the PIC-DEM model is developed in two spatial dimensions (2D).

3

2.1. The PIC model

The present PIC model solves the incompressible Newtonian Navier-Stokes equations for single-phase flow:

$$\nabla \cdot \boldsymbol{u} \; = \; 0 \,, \tag{1}$$

$$\frac{\partial \boldsymbol{u}}{\partial t} + (\boldsymbol{u} \cdot \nabla)\boldsymbol{u} = -\frac{1}{\rho}\nabla p + \nu \nabla^2 \boldsymbol{u} + \boldsymbol{g} \,, \tag{2}$$

where, in 2D, $\boldsymbol{u} = [u, w]^T$ is the velocity field; $\boldsymbol{g} = [0.0, \text{-}9.81 \text{ m/s}^2]^T$ represents the body force due to gravity; p is pressure; t is time, and ν and ρ are the kinematic viscosity and density of the fluid, respectively.

The solution of the governing equations follows the PIC methodology proposed in Brackbill and Ruppel (1986). Both a set of Lagrangian particles and a background Eulerian grid are employed to discretise the computational domain (see Fig. 1). The particles carry the fluid properties such as the mass and momentum, while the background grid is employed solely for computational convenience. During each time step, the velocity field carried by the particles is first mapped onto the grid in a mass and momentum conserving way, and the free-surface location indicated by the particles are also reconstructed on grid. Then, Eq. 1 and Eq. 2, ignoring the advection term (the second term at the left hand side (LHS) of Eq. 2), are solved on the grid for an updated divergence-free velocity field. Finally, the acceleration field (i.e. velocity change between the initially mapped velocity field and the updated divergence-free velocity field) on the grid is interpolated to increment the velocity field carried by the particles and the remaining advection term is solved by moving the particles in a Lagrangian manner. Detailed implementations of these steps are introduced in the works of Chen et al. (2016) (2D version) and Chen et al. (2018) (3D version with domain decomposition based MPI parallelisation). In what follows, only the major components of the PIC model associated with the development of the PIC-DEM model are introduced.

As incompressible flows are assumed, during the solution on the grid a pressure Poisson equation (PPE) is constructed and solved for the fluid pressure. During the solution of the PPE, the boundary conditions for both the free surface and the solid surface are incorporated:

$$p = 0 \quad \text{on } \zeta(\boldsymbol{x}, t), \tag{3}$$

where $\zeta(\boldsymbol{x}, t)$ represents the free-surface position reconstructed on the grid based on the
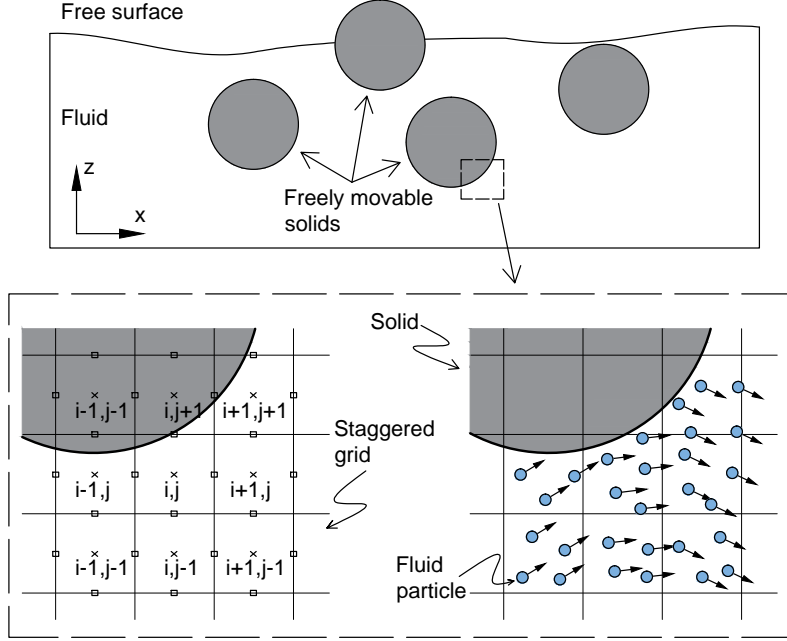
Fig. 1: Sketch of the computational domain, the staggered grid and the fluid particles.

particle position, and

$$\boldsymbol{u} = \boldsymbol{U}_b \quad \text{and} \quad \boldsymbol{n} \cdot (\Delta t \rho^{-1} \nabla p) = \boldsymbol{n} \cdot (\tilde{\boldsymbol{U}}_b - \boldsymbol{U}_b^{n+1}) \quad \text{on } \partial\Omega_S(\boldsymbol{x}, t), \tag{4}$$

where $\partial\Omega_S$ denotes the solid surface; $\boldsymbol{U}_b^{n+1}$ is the velocity on the solid surface at time step $n+1$; $\boldsymbol{n}$ is the unit outward normal vector of the solid surface and $\tilde{\boldsymbol{U}}_b$ represents a tentative velocity on the solid surface. Note that the tentative velocity is not involved in the final solution for the fluid pressure and therefore does not need to be calculated (see Eq. 5 in what follows).

The PPE is discretised and solved in a finite volume sense. Over a fluid cell, G_{ij}, that is partially occupied by a solid (or, in other words, cut by a solid), the discretised PPE can

be expressed by (see detailed derivations in Chen et al. (2016)):

$$
\begin{aligned}
E_{i-\frac{1}{2},j} \cdot \frac{\Delta t(p_{i-1,j}^{n+1} - p_{i,j}^{n+1})}{\rho \Delta x} &+ E_{i+\frac{1}{2},j} \cdot \frac{\Delta t(p_{i+1,j}^{n+1} - p_{i,j}^{n+1})}{\rho \Delta x} \\
&+ E_{i,j-\frac{1}{2}} \cdot \frac{\Delta t(p_{i,j-1}^{n+1} - p_{i,j}^{n+1})}{\rho \Delta z} + E_{i,j+\frac{1}{2}} \cdot \frac{\Delta t(p_{i,j+1}^{n+1} - p_{i,j}^{n+1})}{\rho \Delta z} \\
= E_{i+\frac{1}{2},j} \cdot \tilde{u}_{i+\frac{1}{2},j} - E_{i-\frac{1}{2},j} \cdot \tilde{u}_{i-\frac{1}{2},j} &+ E_{i,j+\frac{1}{2}} \cdot \tilde{w}_{i,j+\frac{1}{2}} - E_{i,j-\frac{1}{2}} \cdot \tilde{w}_{i,j-\frac{1}{2}} - \int_{G_{ij} \bigcap \partial \Omega_S} \boldsymbol{n} \cdot \boldsymbol{U}_b^{n+1} \, dl \,,
\end{aligned}
\tag{5}
$$

where E denotes the length of a cell edge that is not occupied by solids; $\Delta x = \Delta z$ are the grid sizes; dl represents the line differential. Special attention should be drawn to the last term at the right hand side (RHS) of Eq. 5. The velocity integral requires the velocity on the solid surface at the time step $n + 1$, i.e. $\boldsymbol{U}_b^{n+1}$. However, this is unknown at the time step n for freely moving solids. To resolve this issue, the solid velocity $\boldsymbol{U}^{n+1}$ is reinterpreted using the fluid pressures in cells immediately surrounding the solid:

$$
\boldsymbol{U}^{n+1} = \boldsymbol{U}^n + \Delta t \mathbf{M}_s^{-1} \mathbf{J} p^{n+1} + \Delta t \mathbf{M}_s^{-1} (\boldsymbol{F}_g + \boldsymbol{F}_{\text{collision}}),
\tag{6}
$$

where $\boldsymbol{U}^n$ and $\boldsymbol{U}^{n+1}$ are the solid velocities at time steps n and $n + 1$, respectively; Δt is the time step for the fluid solver; $\mathbf{M}_s$ is the mass matrix of the solid; $\mathbf{J}$ is an operator that transfers the fluid pressures to fluid forces, $\boldsymbol{F}_{\text{fluid}}$, on the solid; $\boldsymbol{F}_g$ and $\boldsymbol{F}_{\text{collision}}$ are the external forces due to gravity and solid-solid collisions, of which the latter is computed using the DEM model introduced in the following sections. Once $\boldsymbol{U}^{n+1}$ is constructed, $\boldsymbol{U}_b^{n+1}$ can be reinterpreted straightforwardly to the same components as in Eq. 6 using the law of rigid body motion. When substituting the reconstructed $\boldsymbol{U}_b^{n+1}$ to Eq. 5, the terms associated with $\Delta t \mathbf{M}_s^{-1} \mathbf{J} p^{n+1}$ are moved to the LHS of Eq. 5. This revises only the coefficients of the matrix of the linear system of equations. In such way, the fluid pressure is implicitly resolved for in the PIC model, which makes the model both efficient and stable. For detailed computations of the operator $\mathbf{J}$, the reader is referred to Chen et al. (2016) (in 2D) and Chen et al. (2019) (in 3D).

Once the fluid pressure, p^{n+1}, is obtained on the grid, a divergence-free velocity field on the grid can be calculated using the pressure projection method (Chorin, 1968). As mentioned above, the particles carrying the updated velocity field are then advected through the divergence-free velocity field on the grid. Also, the positions and velocities of the solids are updated at this stage; details are given in Section 2.3.

2.2. The DEM model for solid-solid contact

2.2.1. The contact force calculation

The DEM model presented in Zhang et al. (2009) is slightly modified for the current simulations. The contact forces between two solids are simulated by a spring and dashpot model. In particular, the contact forces and moments acting on a solid i due to a solid j is calculated as:

$$F_{j\to i,\xi}(t) = k_\xi \delta_{ij}(t) + c_\xi U_{ij,\xi}(t) \,, \tag{7}$$

$$F_{j\to i,\eta}(t) = k_\eta \left(U_{ij,\eta}(t)\Delta t_{DEM} \right) + c_\eta U_{ij,\eta}(t) \,, \tag{8}$$

$$M_{j\to i}(t) = F_{j\to i,\eta}(t) R_i \,, \tag{9}$$

where the subscripts ξ and η represent the normal and tangent directions, respectively; k_ξ and k_η are the stiffnesses coefficients in the normal and tangent directions, respectively; c_ξ and c_η are the damping coefficients in the normal and tangent directions, respectively; δ_{ij} is the overlapped distance between the solids i and j; $U_{ij,\xi}$ and $U_{ij,\eta}$ are the relative velocities in the normal and tangent directions, respectively; Δt_{DEM} is the time step used in the DEM modelling and R_i is the arm length. Note that for the spring force in Eq. 8 (i.e. the first term at the RHS), while only one time step displacement in the tangent direction is used here (i.e. $U_{ij,\eta}(t)\Delta t_{DEM}$), an accumulated value of the displacement during the contact is applied in Zhang et al. (2009).

In Eq. 7 and Eq. 8, the stiffness and damping coefficients are calculated as:

$$k_\xi = \frac{m_{ij}\|\boldsymbol{g}\|}{\theta \Delta x} \,, \tag{10}$$

$$c_\xi = 2\alpha\sqrt{m_{ij}k_\xi} \,, \tag{11}$$

$$k_\eta = \frac{k_\xi}{2(1+\psi)} \,, \tag{12}$$

$$c_\eta = \frac{c_\xi}{\sqrt{2(1+\psi)}} \,. \tag{13}$$

In the above equations, $m_{ij} = (m_i + m_j)/2$, where m_i and m_j are the masses of the solids i and j, respectively. However, note that in this paper only solids with an identical mass are simulated, i.e. $m_i = m_j$. θ is a coefficient that controls the penetration length and is set at 1% for all of the simulations in this paper. ψ is the Poisson ratio and α is the tuning parameter.

In addition to Eq. 7-Eq. 13, the following restraints are also enforced during the simula-

tion:

$$F_{j\to i,\xi}(t) = F_{j\to i,\eta}(t) = 0 \quad \text{if } \delta_{ij}(t) = 0 \,, \tag{14}$$

$$|F_{j\to i,\eta}(t)| \leq \mu |F_{j\to i,\xi}(t)| \,, \tag{15}$$

where μ is the maximum static friction coefficient.

The total contact forces and moments acting on the solid i is thus a sum up of all the contact forces due to its neighbouring solids:

$$\boldsymbol{F}_i = \sum_j \boldsymbol{F}_{j\to i} \,, \tag{16}$$

$$\boldsymbol{M}_i = \sum_j \boldsymbol{M}_{j\to i} \,. \tag{17}$$

Also, in order to ensure numerical stability in the DEM simulation, following Zhang et al. (2009) Δt_{DEM} is calculated by:

$$\Delta t_{DEM} = \frac{2\pi}{\gamma} \sqrt{\frac{m_{ij}}{k_\xi}} \,, \tag{18}$$

where γ is set at 150 in the current simulations, which gives a DEM time step similar to that recommended in Robinson et al. (2014). Other recommendations of the coefficient γ can also be found in the open literature (see e.g. Zhang et al. (2009) and Canelas et al. (2016)). Note that typically Δt_{DEM} is smaller than the time step Δt used in the fluid modelling. A coupling algorithm is thus required to deal with the difference between the time steps; this is introduced in Section 2.3.

2.2.2. A gap problem and solution

In the current Cartesian cut cell method based numerical model for fluid-solid interaction (see Section 2.1), it is desired that one computational cell is at most occupied by one solid. It is numerically troublesome and can often lead to numerical instability issue if one computational cell is occupied by multiple solids. On the other hand, it is required by the DEM model that the solids contact and overlap with each other in order to generate the collision forces. In other words, around the contact point the computational cells will be occupied by multiple solids. As a compromise, we propose using an imaginary boundary for each solid (see Fig. 2). Here, it is instead the imaginary boundaries overlapping with each other that gives rise to the contact forces, while ensuring a gap between the real boundaries
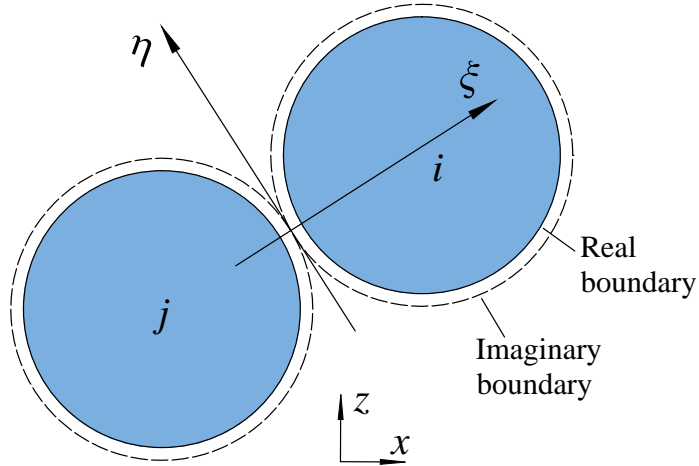
Fig. 2: Sketch showing the contact method in the current DEM model.

of the solids. The gap should be as small as possible when the collision happens. In the current numerical framework, a minimum length of two grid cell sizes is used for the gaps. Thus, for the circular solids presented in Fig. 2 for example, the overlap distance $\delta_{ij}(t)$ is calculated as:

$$\delta_{ij}(t) = \begin{cases} r_i + r_j + 2\Delta x - d_{ij}(t) & \text{if } r_i + r_j + 2\Delta x > d_{ij}(t) \\ 0 & \text{if } r_i + r_j + 2\Delta x \leq d_{ij}(t) \end{cases}, \tag{19}$$

where r_i and r_j are the radii of the circular solids i and j respectively and d_{ij} represents the distance between the centres of the two solids. Note that in case of a solid i contacting with a wall boundary, $\delta_{iw}(t)$ is calculated in the same manner, with r_j set to zero and d_{ij} representing the distance between the centre of solid i and the boundary of the wall.

While the use of the gap resolves the conflict between the cut cell method and the DEM, it is unphysical in principle. One can reduce the grid size or use an adaptive grid configuration to make the numerical gap small, or refer to specific numerical methods targeting on this type of thin gap problem (see e.g. Qiu et al. (2015)). But it may increase the computational cost significantly or introduce additional numerical complexities. We propose a simple method to mitigate this issue based on the understanding that the fluid flow is prevented at the contact area. The contact area is defined as a narrow band area (in 2D) centred at the contact point along the tangent direction of the contact force. The idea is to linearly dissipate the fluid
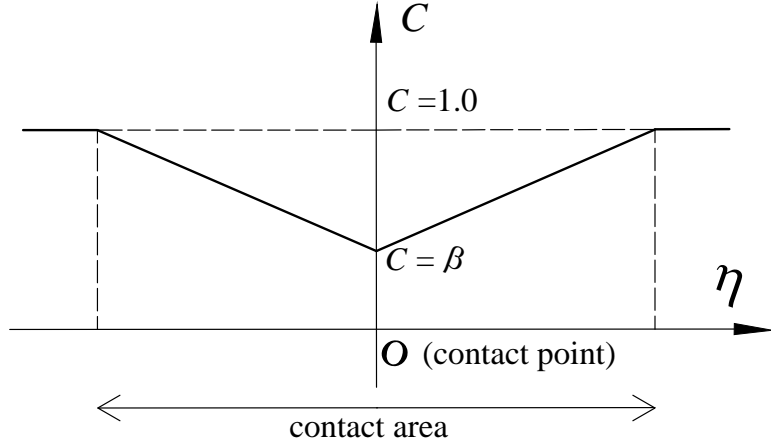
9

Fig. 3: Sketch showing the dissipation function C in the contact area.

velocity carried by the particles who are located within the contact area by:

$$\boldsymbol{v}_p = C_{ij}\boldsymbol{v}_{p,cal} \quad \text{if} \ \delta_{ij}(t) > 0 \,, \tag{20}$$

where $\boldsymbol{v}_{p,cal}$ represents the calculated particle velocity after the fluid step and C is a dissipation function. Fig. 3 shows the function of C. It is designed that outside the contact area C is set to 1.0, while within the contact area C is linearly reduced to β at the contact point. $\beta \in [0,1]$ is a coefficient that can be tuned according to the test cases under consideration. The length of the contact area is set at $4\Delta x$ empirically in the current simulations. In Section 3.2, we show that the use of this approach can effectively improve the simulation results.

2.3. Coupling algorithm of the PIC-DEM model

The major computation of the PIC model for fluid flows is on a fixed Cartesian grid using both finite difference method and finite volume method. Therefore, the characteristic time step of the PIC fluid model is expected to be much larger than that of the DEM model (Zhang et al., 2009). To overcome this difficulty, we employ the idea of using subcycles following Glowinski et al. (1999).

First, Fig. 4 gives an overall algorithm of the coupled PIC-DEM model. It is worth mentioning that as depicted in Fig. 4, during the solution of Eq. 5, the contact force due to solid collisions in Eq. 6 is calculated using the velocities and positions of the solids at the current step (i.e. time level n) as a prediction, which will be recalculated in the DEM part
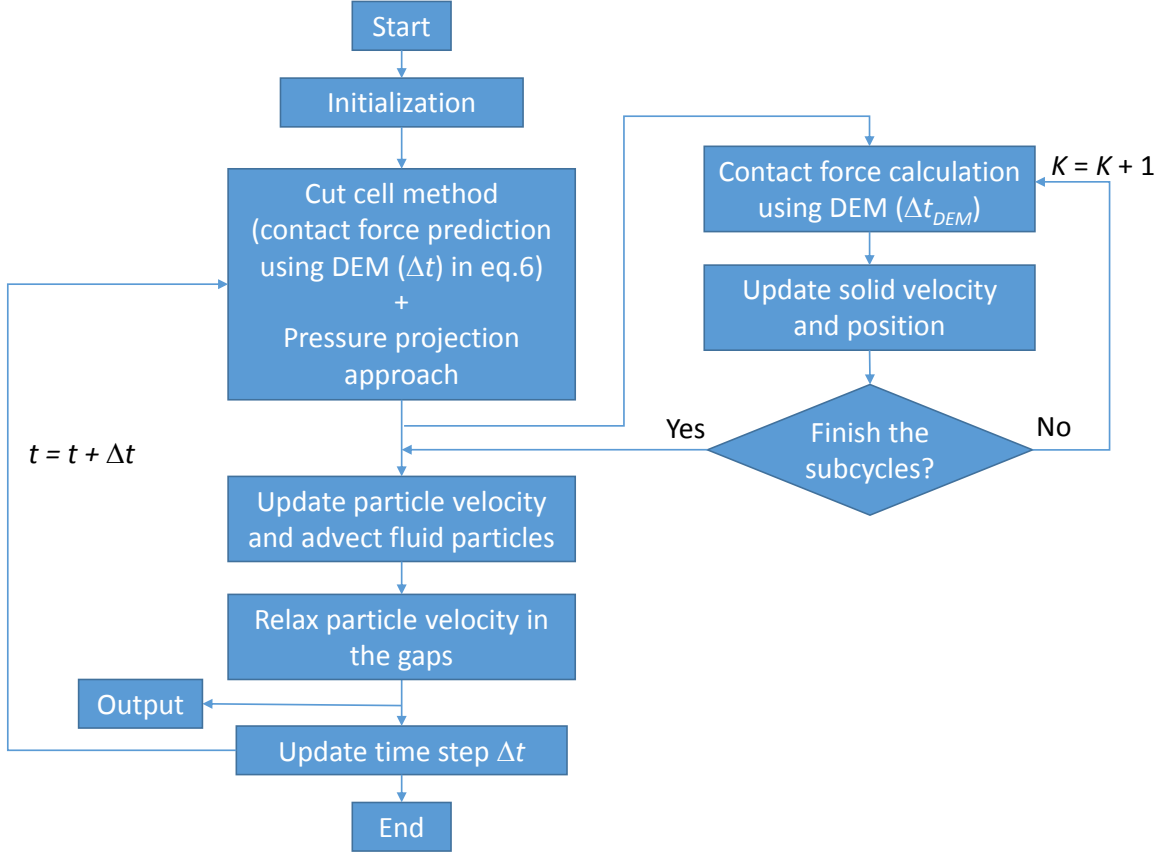
Fig. 4: Schematic showing the coupling algorithm of the PIC-DEM model.

(see below). Note that as this is part of the fluid model, Δt is used in the contact force prediction, instead of Δt_{DEM} (see Eq. 8).

Once the fluid pressure p^{n+1} is solved for, the velocities and positions of the solids are updated in a subcycle manner using the following procedure:

(1) Set $\boldsymbol{U}_0^{n+1} = \boldsymbol{U}^n + \left(\mathbf{M}_s^{-1} F_{\text{fluid}}^{n+1} + \boldsymbol{g}\right)\Delta t$ and $\boldsymbol{X}_0^{n+1} = \boldsymbol{X}^n$;

(2) Do $k = 1, K$

$$\boldsymbol{U}_a^{n+1} = \boldsymbol{U}_{k-1}^{n+1} + \Delta t_{DEM}\mathbf{M}_s^{-1}\boldsymbol{F}_{\text{collision},a}(\boldsymbol{X}_{k-1}^{n+1}, \boldsymbol{U}_{k-1}^{n+1}) \tag{21}$$

$$\boldsymbol{X}_a^{n+1} = \boldsymbol{X}_{k-1}^{n+1} + \left(\frac{\boldsymbol{U}^n + \boldsymbol{U}_a^{n+1}}{2}\right)\Delta t_{DEM} \tag{22}$$

$$\boldsymbol{U}_k^{n+1} = \boldsymbol{U}_{k-1}^{n+1} + \Delta t_{DEM}\mathbf{M}_s^{-1}\left(\frac{\boldsymbol{F}_{\text{collision},a}(\boldsymbol{X}_{k-1}^{n+1}, \boldsymbol{U}_{k-1}^{n+1}) + \boldsymbol{F}_{\text{collision},b}(\boldsymbol{X}_a^{n+1}, \boldsymbol{U}_a^{n+1})}{2}\right) \tag{23}$$

$$\boldsymbol{X}_k^{n+1} = \boldsymbol{X}_{k-1}^{n+1} + \left(\frac{\boldsymbol{U}^n + \boldsymbol{U}_k^{n+1}}{2}\right)\Delta t_{DEM} \tag{24}$$

11

End Do;

(3) Set $\boldsymbol{U}^{n+1} = \boldsymbol{U}_K^{n+1}$ and $\boldsymbol{X}^{n+1} = \boldsymbol{X}_K^{n+1}$.

In the above equations, the subscript k represents the kth subcycle; $\boldsymbol{F}_{\text{fluid}}$ and $\boldsymbol{F}_{\text{collision}}$ are the fluid force and the contact force, respectively; $\boldsymbol{X}$ denotes the position of the solid. The total number of subcycles, K, is calculated as $K = \text{INT}(\Delta t/\Delta t_{DEM})$. In doing so, the DEM time step Δt_{DEM} is modified as $\Delta t_{DEM} = \Delta t/K$. Also, the following condition is imposed for numerical stability:

$$\Delta t_{DEM} = \Delta t \quad \text{if} \ \ \Delta t_{DEM} > \Delta t. \tag{25}$$

3. Results and Discussions

In this section, the DEM model implemented in the PIC-DEM model is first validated against a physical experiment done by Zhang et al. (2009) for the collapse of multiple solid cylinder layers. Following that, the PIC-DEM model is validated using the physical experiment presented also in the above paper for the breaking of a water dam involving multiple solid cylinder layers. Finally, the PIC-DEM model is applied to simulate the fall-pipe solid dumping tests similar to those presented in Chen (2017).

3.1. Validation of the DEM model

The DEM model is verified using the experiment for the collapse of multiple solid cylinder layers performed by Zhang et al. (2009), with the aim to determine the appropriate values for the coefficients mentioned in Section 2.2. Fig. 5 shows a sketch of the setup of the
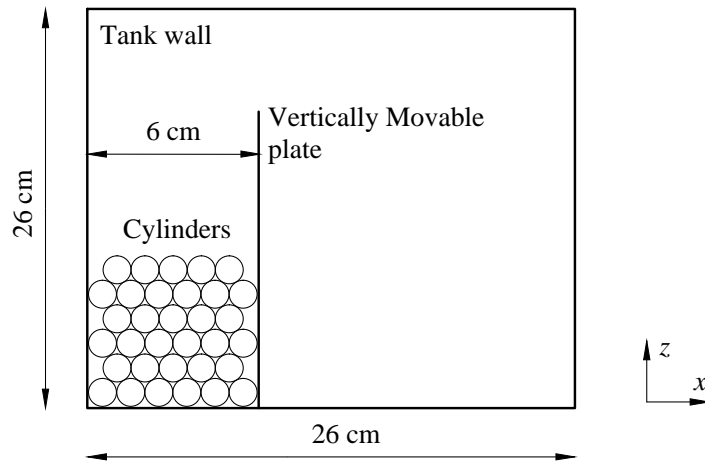

Fig. 5: Schematic showing the setup of the experiment for the collapse of multiple solid cylinder layers.

Table 1: The DEM parameters used in the simulation.

Parameters	Values
Damping coefficient α	0.4
Poisson ratio ψ	0.3
Maximum static friction coefficient μ	0.3

experiment. As seen from Fig. 5, layers of solids with five or six cylinders are alternatively piled up against the LHS wall of a tank and a movable plate. During the experiment, the plate was pulled out vertically upwards, causing the cylinder layers to collapse due to gravity. The tank was 26 cm long, 10 cm wide and 26 cm high. The distance between the left wall and the plate was 6 cm. The solid cylinders were made of aluminum with a density of 2.7×10^3 kg/m^3. The cylinders were identical and had a diameter of 1.0 cm and a length of 9.9 cm, which makes this test case a 2D problem in principle. Note that different numbers of layers of cylinders were tested in the experiment, and for the current DEM model validation, six layers of cylinders are used as seen from Fig. 5. For full details of the setup of the experiment, the reader is referred to Zhang et al. (2009).

In terms of the numerical simulation, Table 1 gives a list of all the parameters tuned by the experiment. Also, in the simulation, despite that no fluid is involved, the background computational grid size is set to $\Delta x = \Delta z = 0.05$ cm, which leads to approximately 20 cells across the diameter of the cylinder. This number of cells is recommended by our previous grid convergence study on simulating wave interaction with a fixed cylinder using the PIC model (Chen et al., 2016). Note that because the PIC-DEM model uses a gap of approximately $2\Delta x$ wide (i.e. 0.1 cm in this test case) between the cylinders, the initial overall length of the cylinder layers (in the x-direction) is larger than 6 cm as in the experiment (see Fig. 5). Therefore, in the numerical simulation the tank size is enlarged correspondingly by a factor of 1.1. In addition, the plate is not simulated in the numerical model.

Fig. 6 shows a comparison between the experimental and numerical results. It can be seen that the numerical model reproduces well the behaviour of the cylinders. Fig. 7 further compares the transient average location of the mass centres of the cylinders. The average location of the mass centres is calculated by:

$$\boldsymbol{x}_{ave} = \frac{\sum_{i=1}^{N} \boldsymbol{X}_i}{N} . \tag{26}$$

Again, it can be seen from Fig. 7 that the numerical predictions agree well with the experimental observations. In short summary, the numerical results provide confidence for the
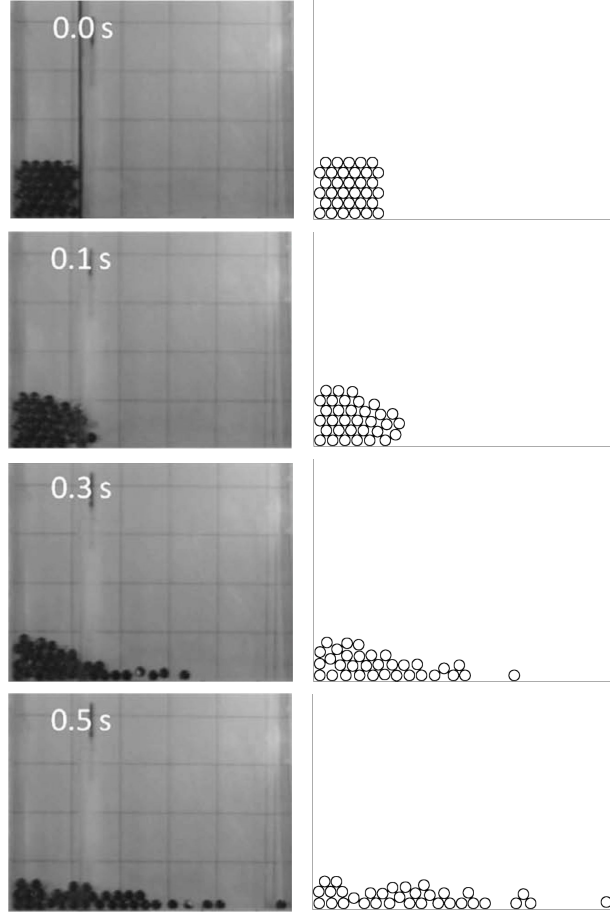
Fig. 6: Comparison between the experimental and numerical results for the collapse of six solid cylinder layers. Left: experimental photography, reprinted from Zhang et al. (2009), Copyright (2009), with permission from Elsevier; Right: snapshots of the present numerical results.

DEM model, as well as the tuned parameters, to be used in the fluid-solid mixture flow tests.

3.2. Validation of the fluid-solid PIC-DEM model

The coupled PIC-DEM model is verified by the experiment for the breaking of a water dam involving multiple solid cylinder layers. In this test case, the cylinders are piled up in the same manner as that used for validating the DEM model. However, the area between the left wall of the tank and the movable plate is filled with water ($\rho = 1.0 \times 10^3$ kg/m^3, $\nu = 1.0 \times 10^{-6}$ m^{2}s^{-1}). The height of the water dam is fixed at 12 cm, and 6, 8, 10 and 12 layers of solid cylinders are tested.

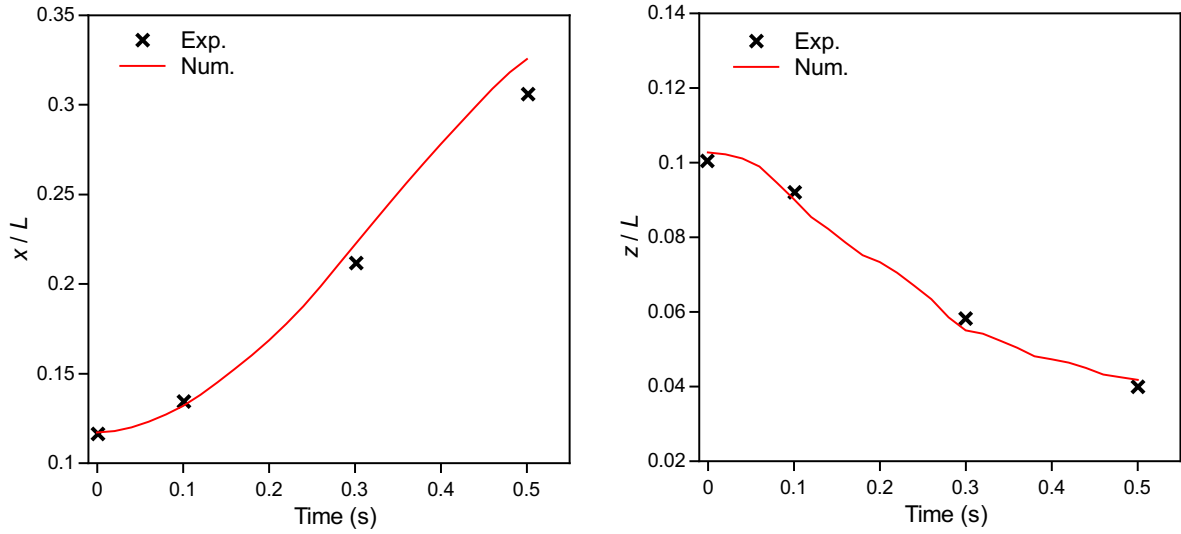For the setup of the numerical model, the grid size and the DEM parameters are all

Fig. 7: Comparisons for the time histories of the location of the average mass centres for the collapse of six solid cylinder layers. Left: in the horizontal direction; Right: in the vertical direction. L represents the tank length. The experimental data are digitised from Zhang et al. (2009).

kept the same as those used in the above solids only test. Also, numerical simulations with and without the solution for the gap problem discussed in Section 2.2.2 are both run for comparison.

Fig. 8 and Fig. 9 show the breaking of the water dam involving 6 and 12 layers of cylinders over time, respectively. Comparisons are made amongst the experimental observations, numerical results with the gap solution (with $\beta = 0.5$, see Fig. 3) and numerical results without the gap solution (i.e. $\beta = 1.0$). It can be seen that with the gap solution, the numerical results match well with the experimental observations, while without the solution the cylinders are rushed towards the RHS wall of the tank more easily as water can flow past the gaps more easily. This clearly demonstrates the effectiveness of the solution proposed in Section 2.2.2 for the gap problem. Furthermore, it can be seen from Fig. 8 and Fig. 9 that the numerical model (with gap solution, $\beta = 0.5$) captures both the cylinder motion and the free-surface deformation reasonably well. It is also interesting to note that in the 12 layers case the dam-break flow appears much less violent than that in the 6 layers case.

Finally, Fig. 10 presents the results of the arrival time of the cylinders, which is defined as the first instance of a cylinder coming into contact with the RHS wall of the tank. The numerical results in general agree well with the experimental data, considering the complexity of this test case and the time scale (within half a second).
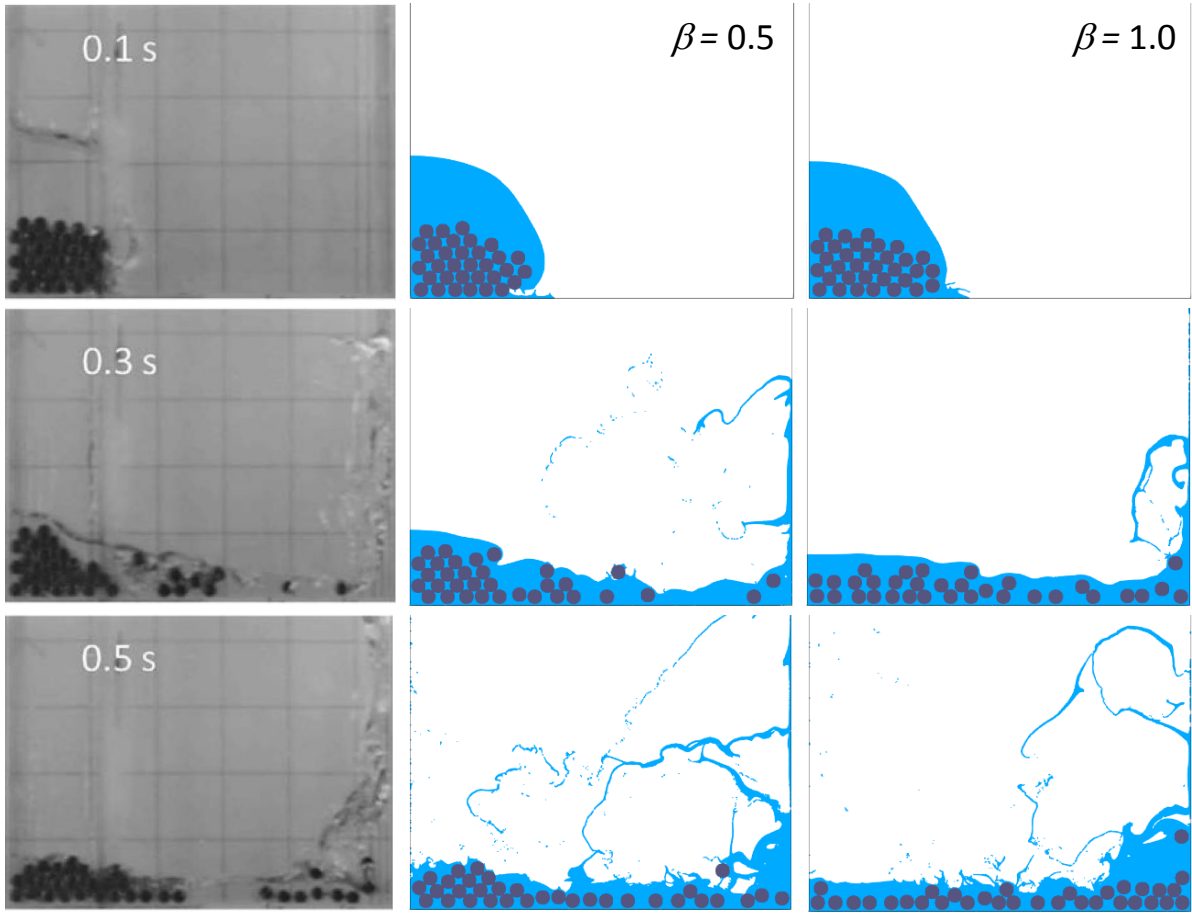
15

Fig. 8: Comparison between the experimental and numerical results for the breaking of a water dam involving six solid cylinder layers. Left: experimental photography, reprinted from Zhang et al. (2009), Copyright (2009), with permission from Elsevier; Middle: snapshots of the present numerical results with gap solution; Right: snapshots of the present numerical results without gap solution.

3.3. Application to a fall-pipe solid dumping test

In this section, the coupled PIC-DEM model is applied to a fall-pipe solid dumping test. Fig. 11 shows a sketch of the setup of the numerical simulation. This test case is an extension to the validation case of the fluid-solid mixture flow. The tank is now fully filled with water (in the x-direction) with the same water depth as above. Here, the cylinders are initially piled in the middle of the tank just above the still water level (S.W.L) and, particularly, inside a vertical pipe with a funnel on the top (see Fig. 11). During the simulation, the cylinders fall through the pipe onto the bottom of the tank due to gravity. This test case resembles the targeted placement of rocks onto the sea bed for the protection of offshore pipelines and cables and scour protection for windfarm structures (Beemsterboer, 2013). The idea is to numerically test the productivity of fall-pipe solid dumping and to demonstrate the capability of the current numerical model on handling such a complex fluid-solid interaction
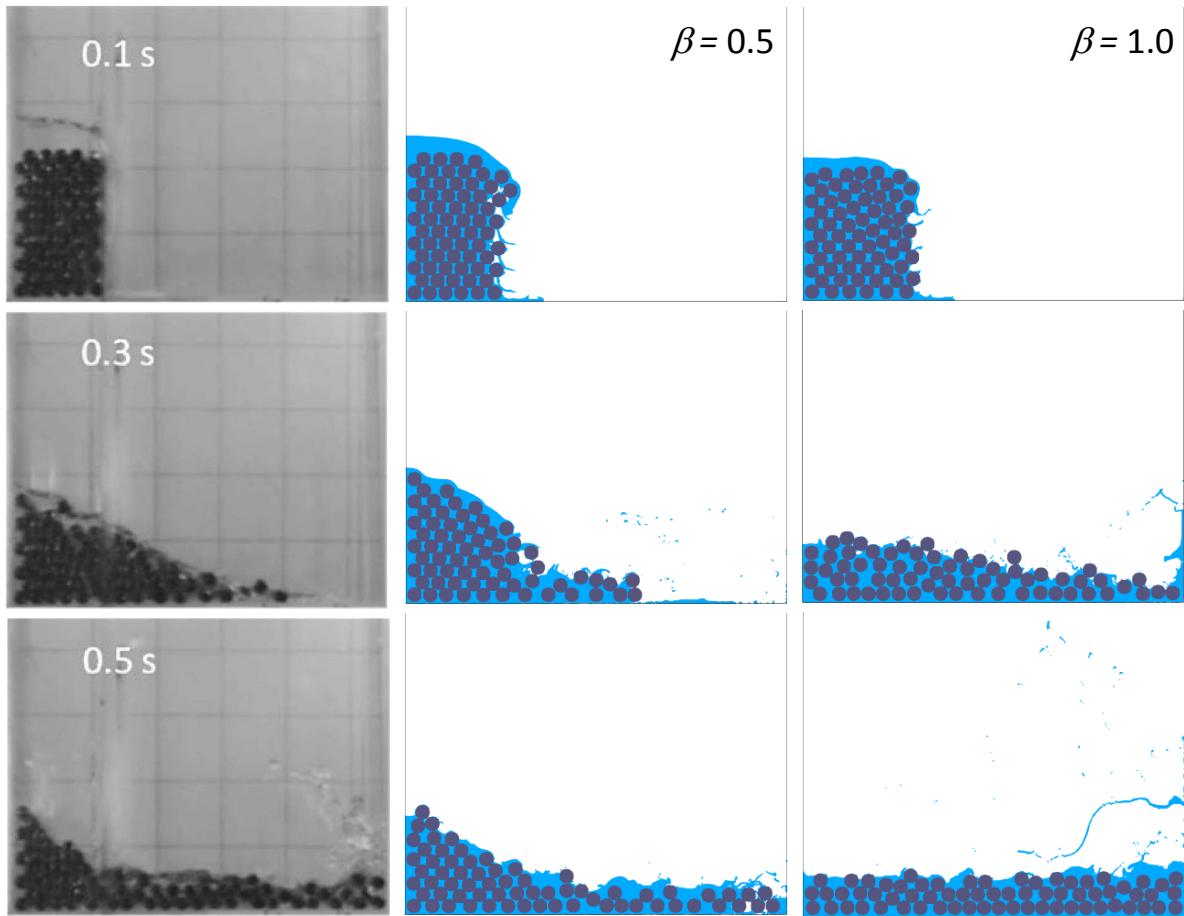
16

Fig. 9: Comparison between the experimental and numerical results for the breaking of a water dam involving twelve solid cylinder layers. Left: experimental photography, reprinted from Zhang et al. (2009), Copyright (2009), with permission from Elsevier; Middle: snapshots of the present numerical results with gap solution; Right: snapshots of the present numerical results without gap solution.

scenario.

All of the numerical parameters of the PIC-DEM model are kept the same as those used for the validation case in Section 3.2. The boundary conditions of the vertical fall pipe are set the same as those of the tank walls. Six layers of cylinders with an alternative five or six cylinders per layer are simulated (see Fig. 11).

In addition to the continuous pipe as seen in Fig. 11, a perforated pipe, resembling semi-open fall-pipes (Beemsterboer, 2013), is also simulated for comparison. In particular, the perforated pipe has a small hole (0.1 cm wide) on the pipe walls every 2 cm from the bottom to the top. Fig. 12 shows a comparison for the cylinder and water behaviours over time using the continuous and the perforated pipes, respectively. Focusing on the continuous pipe first (Fig. 12(A1-A5)), it can be seen that as the cylinders fall through the pipe, a downward flow is generated, leading to a decrease of the water level inside the pipe while a increase
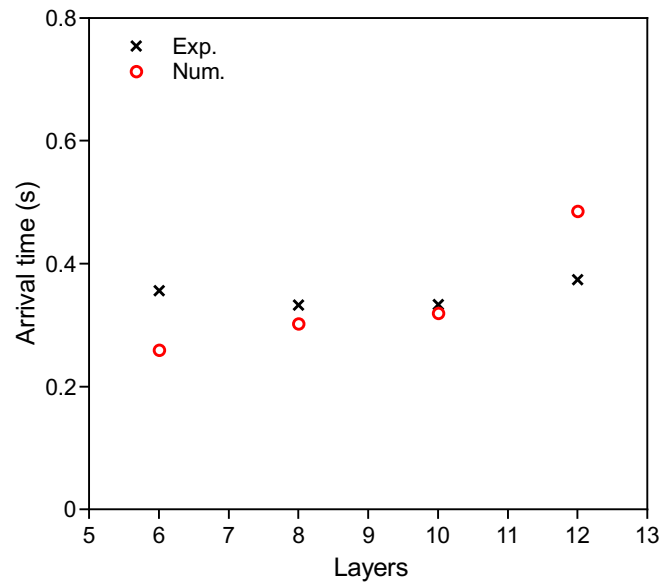
Fig. 10: Comparison for the arrival time of the cylinders to the RHS wall of the tank. The experimental results are digitised from Zhang et al. (2009).
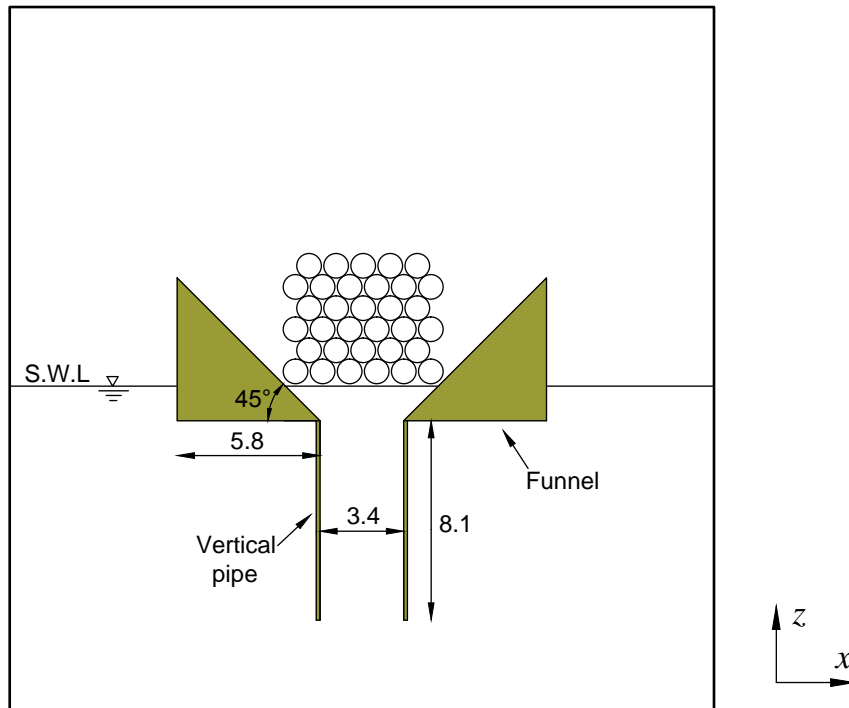

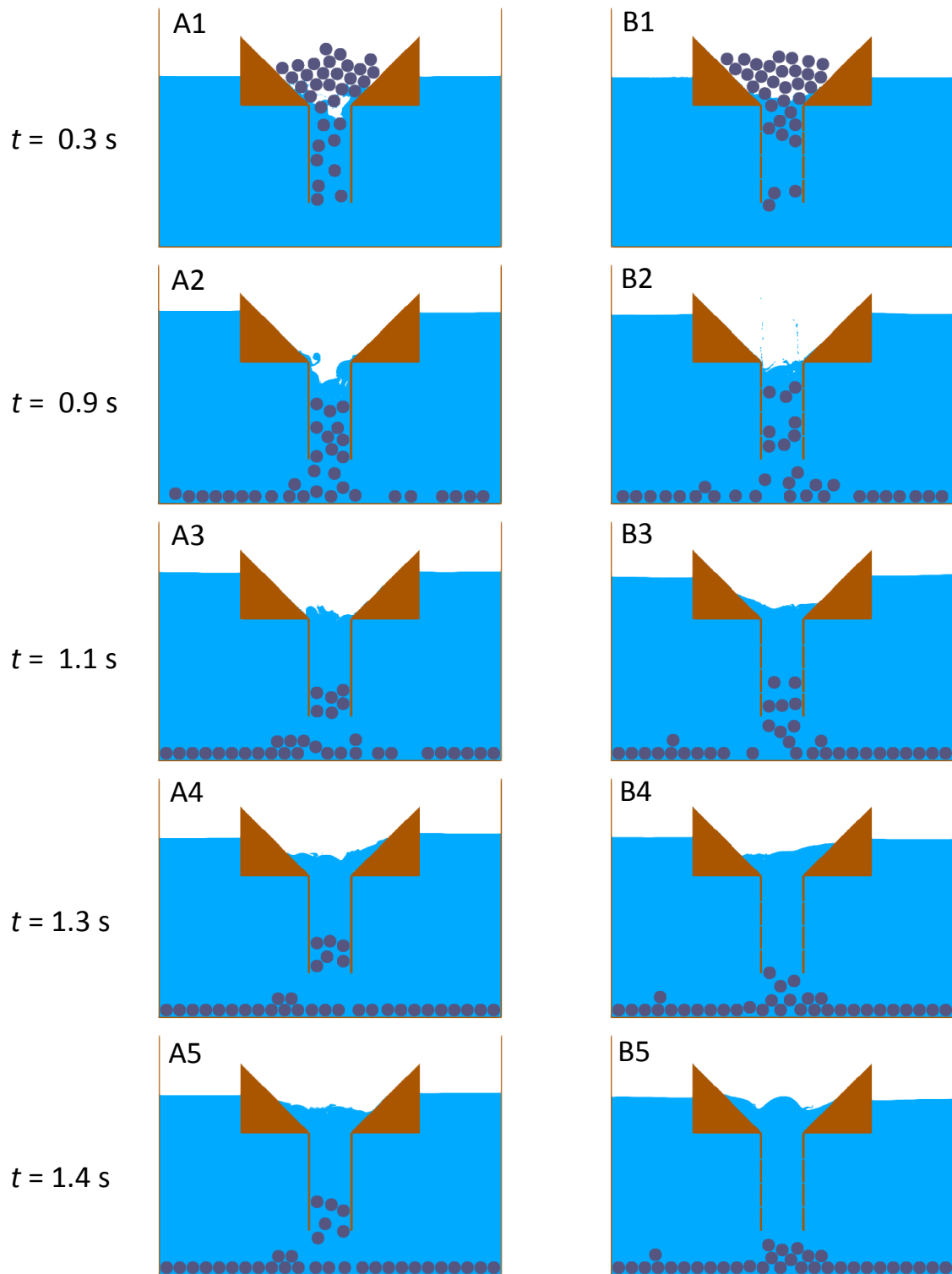Fig. 11: Sketch of the setup of the numerical simulation (Unit: cm).

Fig. 12: Snapshots of the numerical results for the fall-pipe solid dumping tests using the continuous pipe (A1-A5) and the perforated pipe (B1-B5).
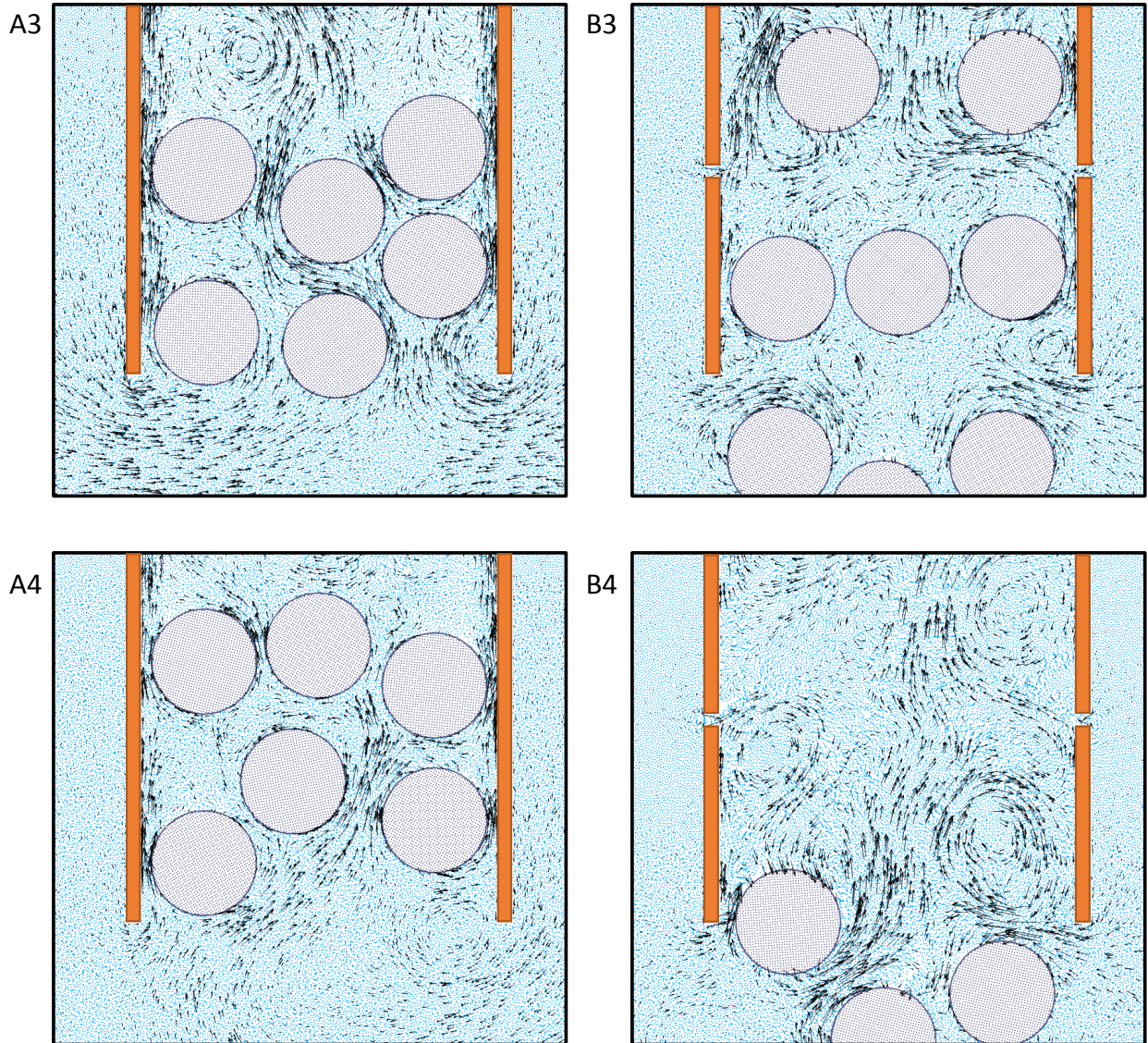
Fig. 13: The velocity field around the bottoms of the fall pipes. Left: the continuous pipe case, figures correspond to Fig. 12(A3)-(A4); Right: the perforated pipe case, figures correspond to Fig. 12(B3)-(B4).

of the water level outside the pipe (Fig. 12(A1-A2)). The continuously growing imbalanced water levels later on cause a reversed flow (i.e. upward) inside the pipe (Fig. 12(A3-A5)), which slows down and even lifts up the cylinders slightly. This eventually leads to a delay of the solid dumping. Looking at the perforated pipe case in comparison (Fig. 12(B1-B5)), the cylinders are quickly dumped out without delay. Although the reversed flows are also observed here, they are not as continuous as those seen in the continuous pipe, due to an equalisation of the fluid pressure inside and outside the perforated pipe via flows through

the holes. Fig. 13 further shows the velocity field around the bottom of the pipe, which confirms the above discussions.

4. Conclusions

In this study, a coupled PIC-DEM model is developed and validated for numerical simulations of complex fluid-solid mixture flows. Although the test cases of the collapse of solid cylinder layers are very complicated, the predictions of the numerical model agree well with the results of physical experiments. The more complex test case of dumping solid cylinders through fall pipes further demonstrates the capability of the numerical model. These show that the proposed coupling algorithm for the PIC and the DEM models works well, with the idea of using subcycles to handle the time step difference. The results also verify the proposed cheap solution for the unphysical gaps during solid collisions that are due to the Cartesian cut cell method for fluid-solid interaction. Nevertheless, the coefficient β requires calibration as other DEM parameters. Furthermore, although the PIC-DEM model is developed in 2D, it should be straightforward to extend the model to 3D. Also, extension on the DEM model could be exploited for simulations of fluid interaction with arbitrary shape solids. Overall, with further innovations and developments, the coupled PIC-DEM model could become a useful tool for other similar applications in the coastal and offshore engineering field.

References

Beemsterboer, T. N., 2013. Modelling the immediate penetration of rock particles in soft clay during subsea rock installation, using a flexible fallpipe vessel. Master Thesis for the Technical University of Delft.

Brackbill, J. U., Ruppel, H. M., 1986. FLIP: A method for adaptively zoned, Particle-In-Cell calculations of fluid flows in two dimensions. J. Comp. Phys. 65, 314–343.

Canelas, R. B., Crespo, A. J. C., Domínguez, J. M., Ferreira, R. M. L., Gómez-Gesteira, M., 2016. SPH-DCDEM model for arbitrary geometries in free surface solid-fluid flows. Computer Physics Communications 202, 131 – 140.

URL http://www.sciencedirect.com/science/article/pii/S0010465516000254

Chen, Q., 2017. Development of a full particle pic method for simulating nonlinear wave-structure interaction. Ph.D. thesis, University of Bath.

Chen, Q., Zang, J., Dimakopoulos, A. S., Kelly, D. M., Williams, C. J., 2016. A Cartesian cut cell based two-way strong fluid-solid coupling algorithm for 2D floating bodies. Journal of Fluids and Structures 62, 252 – 271.

URL http://www.sciencedirect.com/science/article/pii/S0889974616000153

Chen, Q., Zang, J., Kelly, D. M., Dimakopoulos, A. S., 2018. A 3D parallel particle-in-cell solver for wave interaction with vertical cylinders. Ocean Engineering 147, 165 – 180.

Chen, Q., Zang, J., Ning, D., Blenkinsopp, C., Gao, J., 2019. A 3D parallel particle-in-cell solver for extreme wave interaction with floating bodies. Ocean Engineering 179, 1 – 12.

URL http://www.sciencedirect.com/science/article/pii/S002980181831504X

Chorin, A. J., 1968. Numerical solution of the Navier–Stokes equations. Math. Comput. 22, 745–762.

Cundall, P. A., Strack, O. D. L., 1979. A discrete numerical model for granular assemblies. Géotechnique 29 (1), 47–65.

URL https://doi.org/10.1680/geot.1979.29.1.47

Edwards, E., Bridson, R., 2012. A high-order accurate Particle–In–Cell method. International Journal for Numerical Methods in Engineering 90 (9), 1073–1088.

URL http://dx.doi.org/10.1002/nme.3356

Glowinski, R., Pan, T.-W., Hesla, T., Joseph, D., 1999. A distributed Lagrange multiplier/fictitious domain method for particulate flows. Int. J. Multiphase Flow 24, 755–794.

Guo, Y., Curtis, J. S., 2015. Discrete element method simulations for complex granular flows. Annual Review of Fluid Mechanics 47 (1), 21–46.

URL https://doi.org/10.1146/annurev-fluid-010814-014644

Harlow, F. H., 1964. The Particle–In–Cell computing method for fluid dynamics. In: Alder, B. (Ed.), Methods in Computational Physics. Academic Press, New York, pp. 319–343.

He, Y., Bayly, A. E., Hassanpour, A., Muller, F., Wu, K., min Yang, D., 2018. A GPU-based coupled SPH-DEM method for particle-fluid flow with free surfaces. Powder Technology 338, 548 – 562.

URL http://www.sciencedirect.com/science/article/pii/S0032591018305424

Koshizuka, S., Oka, Y., 1996. Moving-particle semi-implicit method for fragmentation of incompressible fluid. Nuclear Science and Engineering 123 (3), 421–434.

URL https://doi.org/10.13182/NSE96-A24205

Maljaars, J. M., Labeur, R. J., Möller, M., 2018. A hybridized discontinuous galerkin framework for high-order particlemesh operator splitting of the incompressible navierstokes equations. Journal of Computational Physics 358, 150 – 172.

URL http://www.sciencedirect.com/science/article/pii/S0021999117309300

Patankar, N. A., Singh, P., Joseph, D. D., Glowinski, R., Pan, T.-W., 2000. A new formulation of the distributed lagrange multiplier/fictitious domain method for particulate flows. International Journal of

Multiphase Flow 26 (9), 1509 – 1524.

URL http://www.sciencedirect.com/science/article/pii/S0301932299001007

Qiu, L., Yu, Y., Fedkiw, R., 2015. On thin gaps between rigid bodies two-way coupled to incompressible flow. Journal of Computational Physics 292, 1 – 29.

URL http://www.sciencedirect.com/science/article/pii/S0021999115001746

Robinson, M., Ramaioli, M., Luding, S., 2014. Fluid-particle flow simulations using two-way-coupled mesoscale SPH-DEM and validation. International Journal of Multiphase Flow 59, 121 – 134.

URL http://www.sciencedirect.com/science/article/pii/S0301932213001882

Violeau, D., Rogers, B. D., 2016. Smoothed particle hydrodynamics (SPH) for free-surface flows: past, present and future. Journal of Hydraulic Research 54 (1), 1–26.

URL https://doi.org/10.1080/00221686.2015.1119209

Zhang, C., Su, P., Ning, D., 2019. Hydrodynamic study of an anti-sloshing technique using floating foams. Ocean Engineering 175, 62 – 70.

URL http://www.sciencedirect.com/science/article/pii/S0029801819300502

Zhang, S., Kuwabara, S., Suzuki, T., Kawano, Y., Morita, K., Fukuda, K., 2009. Simulation of solid-fluid mixture flow using moving particle methods. Journal of Computational Physics 228 (7), 2552 – 2565.

URL http://www.sciencedirect.com/science/article/pii/S0021999108006499